Measuring geometric imperfections of variable–angle filament–wound cylinders with a simple digital image correlation (DIC) set up

Saullo G. P. Castro[a,∗], José Humberto S. Almeida Jr.[b,∗], Luc St-Pierre[b] and Zhihua Wang[a,c]

[a]*Faculty of Aerospace Engineering, Delft University of Technology, Delft, The Netherlands*
[b]*Department of Mechanical Engineering, Aalto University, Espoo, Finland*
[c]*School of Mechanical and Electrical Engineering, University of Electronic Science and Technology of China, Chengdu, China*

ARTICLE INFO

ABSTRACT

The experimental measurement of geometric imperfections of cylindrical shells is a fundamental step towards achieving representative models that are capable of capturing the imperfection-sensitive behavior of this type of shells and generate predictions that are comparable with experimental tests. The present study proposes an imperfection measurement method that is simple and applicable to both small and large structures, whereby the topographic data measured with one pair of cameras is obtained at six circumferential positions. Practical aspects of using digital image correlation are discussed, such as lighting and focus adjustments, and calibration. State-of-the-art best-fit routines are used to transform the obtained raw imperfection data onto a common coordinate system by means of least-squares optimization steps. Finally, the transformed data is stitched to build the full imperfection patterns that can be readily used in nonlinear finite element analyses. The developed method is demonstrated in the present study by measuring 12 variable-angle filament-wound cylinders, a novel class of variable-stiffness structures developed by our research group that combines a wide tailoring capability coming from the variable stiffness with the efficient manufacturability enabled by the filament winding process.

Highlights

- Discussed important practical aspects of digital image correlation systems
- Achieved experimentally measured geometric imperfections with a simple set up
- Applied the developed method to 12 variable-angle filament-wound cylinders

1. Introduction

The buckling performances of thin-walled structures can be significantly affected by uncertainties coming from load definitions, material properties, geometric variables and boundary conditions [1]. Fiber-reinforced composite materials are often employed in primary aeronautical and aerospace components because of their outstanding specific strength and stiffness, corrosion resistance, and high tailorability that allows design solutions not achievable with metals [2]. Aerospace structures usually consist of thin-walled shells that can buckle when subject to compressive loads. Curved shells, especially cylinders, can build a high membrane stress level under compression before buckling, becoming peculiarly sensitive to geometric imperfections [3]. This phenomenon was first observed by Southwell [4] in 1914, when isotropic cylindrical shells were found to buckle at considerably lower loads than theoretically predicted (for geometrically perfect cylinders). The first buckling design criteria for imperfect structures were proposed by Flügge

[5] and Donnell [6], but these guidelines were mainly based on empiricism. The classical reports from von Kármán and Tsien [7] and Koiter [8] confirmed the assumption that initial geometric imperfections, as deviations from an idealized geometry, are the primary source of discrepancy between predictions and experiments. These empirical factors, created to penalize the geometry and then referred to as knockdown factors (KDF), were applied with the objective of reducing the conservative predictions for the load carrying capacity. Although recognizably conservative, this method is still largely applied in preliminary design, such as with the NASA SP-8007 [9].

The first work on imperfect fiber-reinforced composite shells was reported by Sheinman and Simitses [10]; their analytical model included axisymmetric-type geometric imperfections. They concluded that the imperfection sensitivity of orthotropic shells in axial compression decreases with both increasing radius-to-thickness (r/t ratio) and length-to-thickness (l/t ratio) values. Their assumptions were later confirmed [11] with axial compression tests on boron/epoxy composite cylinders [12]. Nevertheless, these assumptions were still considered as semi-empiric. The first direct measurement of geometric imperfections was reported by Chryssanthopoulos et al. [13] for aramid/epoxy composite cylinders. They employed a linear voltage displacement transducer (LVDT) to measure inner and outer surfaces, in which

∗Corresponding Author
✉ S.G.P.Castro@tudelft.nl (S.G.P. Castro); humberto.almeida@aalto.fi (J.H.S. Almeida Jr.); luc.st-pierre@aalto.fi (L. St-Pierre); zhwanglbb@gmail.com (Z. Wang)
ORCID(s): 0000-0001-9711-0991 (S.G.P. Castro); 0000-0002-9408-7674 (J.H.S. Almeida Jr.); 0000-0003-3857-5398 (L. St-Pierre); 0000-0001-8930-4817 (Z. Wang)

the imperfections were recorded in an interval of 10 mm axially and 20 mm circumferentially. The external surface of the cylinder was adjusted using the so called "best-fit" procedure originally proposed by Arbocz and Babcock [14]. Thenceforth, the number of reports and methods increased substantially and it is well established that considering imperfections is vital to accurately predict the actual load carrying ability of shells [15].

One of the most disseminated methods to consider imperfections is the linear buckling mode-shape imperfections (LBMI), initially proposed by Khot and Venkayya [16], who used axisymmetric mode-shapes obtained through linear buckling analysis as geometric imperfections in the nonlinear analysis [17]. An advantage of the LBMI method is that the imperfection pattern is obtained from a computationally–cheap eigenvalue buckling analysis and it is straightforward to include such imperfections as an initial state to create a load path to reach the post-buckling state [18]. Another recent but perhaps equally well–disseminated approach to take imperfections into account is the "single perturbation load approach (SPLA)", originally proposed by Hühne et al. [19], which consists of applying a lateral load prior to the axial compression, whose load stimulates a single buckle during the following axial compression. However, the SPLA does not consider other types of imperfections, e.g. load asymmetries [20]. Although LBMI, SPLA, and axisymmetric imperfection approaches can be realistic for shells with well-known or smooth surfaces, they can provide, nevertheless, inaccurate predictions for structures with complex architecture, such as modern cylinders with variable–angle tow (VAT) and/or variable–thickness character [21] produced via advanced manufacturing techniques, such as filament winding. In such case, a suitable method to account for imperfections towards less conservative KDFs would be by means of real–measured mid–surface imperfection (MSI) and thickness–imperfections approaches [22].

Degenhardt et al. [23] carried out an in-depth imperfections measurement of carbon fiber–reinforced polymer (CFRP) unstiffened cylinder. Firstly, they checked the cylinder using an automatic ultrasonic testing using water split coupling to detect any defects in the structure. This method can also be used to take full field thickness measurements. They scanned the imperfections, nevertheless, using an optical 3D digitizing system based on photogrammetry to extract the actual radius of the structures and the initial geometric imperfections, both using the best–fit procedure. They used four high–speed cameras simultaneously to scan the whole cylinder, each covering 90°of the shell. Although a precise measurement system, it is very expensive and a complex assembly of the whole system is needed. This system was successfully employed by Khakimova et al. [24] to measure thickness imperfections of unstiffened CFRP cylinders, also using the best–fit method. Eberlein [25] measured imperfection signature of CFRP cylinders using light scanner, system also used by NASA. The measurements resulted in a KDF of 0.91, much less conservative than the KDF using NASA SP-8007 guideline, which was of 0.59, where a

precise and robust imperfections measurement played a key role. Another approach is by using laser scanner, as carried out by Skukis et al. [26]. The best-fit-cylinder algorithm was used to eliminate rigid body motion odes from the measurements. However, their method was not able to cover 360° of the cylinder and an error of 15% between experiments and predictions was found. Labans and Bisagni [27] measured imperfections of VAT cylinders using a hybrid system, in which the outer surface was scanned using digital image correlation (DIC) system, and the inner surface using laser distance sensor. As a key achievement, they found out that VAT cylinders are less sensitive to geometric imperfections than constant–stiffness cylinders. Then, some conclusions from these studies can be drawn:

- experimental imperfections measurement set ups are very expensive and complex;

- there is still not a well established procedure to capture 360° of a 3D structure; and

- all camera–based systems have at least two cameras to scan the whole circumference of the cylinder.

In addition to these identified issues, it is well–established that filament winding [28] is the most suitable and fastest manufacturing method to produce composite cylinders. Moreover, after the very first report in the literature on VAT filament–wound cylinders carried out by Wang et al. [21], on reliability–based design and optimization, it becomes evident that real geometric imperfections and their effects on the mechanical performance of filament–wound shells is yet unknown and unexplored. Almeida Jr. et al. [29] demonstrated the superior tailoring potential and mechanical properties of VAFW cylinders.

Therefore, this work aims at overcoming all these issues by proposing an original and less costly methodology to measure geometric imperfections of variable–angle filament–wound (VAFW) composite cylinders through DIC using only one pair of stereo cameras, still being able to cover the whole circumference of the structure. The methodology on how to stitch each individual measurement to reconstruct the full shell imperfection is described. First, a new best–fit algorithm is developed to accurately determine the outer surface of the cylinder for each measurement. Thus, each measurement is rotated and the adjacent imperfection data compared to determine the exact rotation angle that perfectly stitches each measurement. After trimming each rotated measurement, the complete shell imperfection is achieved.

2. Digital Image Correlation (DIC) System

Digital Image Correlation (DIC) consists of an optical method mostly used to measure deformations on a surface of a 3D object. The method tracks the gray value pattern in small neighborhoods called subsets during deformation. Digital Image Correlation has been proven over and over to be accurate when compared to valid FE models. The

commercially available VIC-2D and VIC-3D systems from isi-sys Optical Measurement Solutions GmbH [30] both utilize this advanced optical measurement technology. For the present study, a pair of 9 mega-pixel cameras with 50mm lenses are used.

3. Imperfection Measurements

Cylinders and Speckle Patterns

The set of four cylinders named MA, CA, VAFW4 and VAFW8 were manufactured in triplicate and are shown in Figure 2. The cylinders are cast into a metal–filler toughened epoxy resin for improved load distribution in later compression tests (Figure 1). After casting, all cylinders undergo painting starting with a white layer and followed by a speckle pattern application. There is a considerable difference between the speckle patterns for the different sample, as shown in Figure 3. For instance, cylinder VAFW4-1 and MA-2 have almost no speckles, whereas MA-1, CA-3, VAFW4-2, VAFW4-3, VAFW8-1 and VAFW8-2 have a rather dense speckle pattern. All other samples have patterns within this qualitative range. The size of the speckles was kept small to prevent loss of imperfection data, and the authors tried always to achieve smaller patterns. In all cases, the speckle painting is performed by positioning the black painting spray at about 0.5 m away from the cylinders, pointing it slightly tangentially to the cylinder and gently pressing the spray nozzle. The exhaustion air assisted to carry the painting mist towards the cylinder.
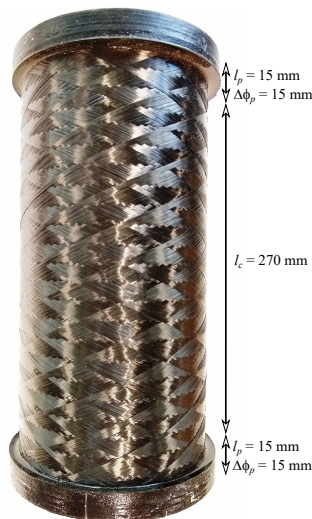

Figure 1: Resin potting details, where l_c is the cylinder length, l_p is the resin potting length, and $\Delta\phi_p$ is the potting diameter variation.

Figure 2: Filament-wound cylinders used in the imperfection measurements. Outer diameter: 136mm; length including resin casting: 300 mm; shell nominal thickness: 0.8 mm; resin casting cross section: 15×15 mm.

Figure 3: Speckle patterns applied to each FW cylinder. Sparse and dense speckle patterns were tried, avoiding large black areas to prevent loss of measured imperfection data.

Setting up the DIC System

The DIC cameras are mounted at about 700 mm distant from the cylinder. A sturdy table is used to support the cylinders during the measurements. The vertical position of the cameras is adjusted such that the lenses stay at the same 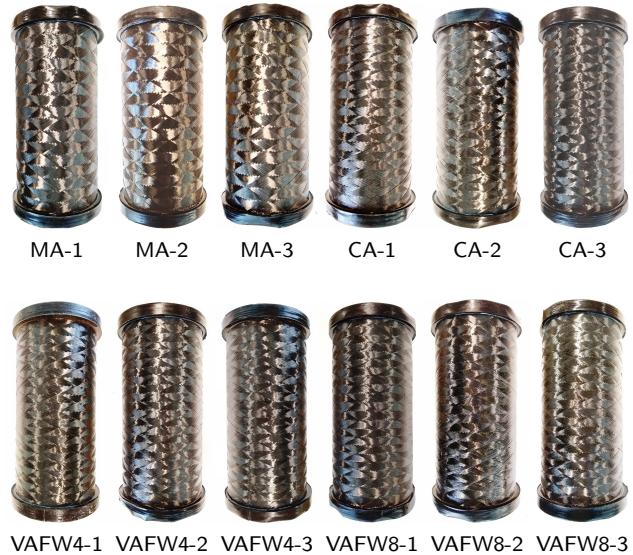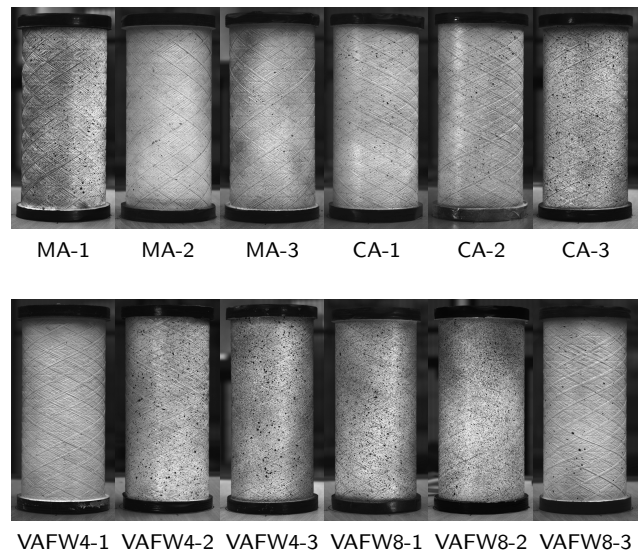height as the middle cross section of the cylinders. The computer is placed in a convenient way to look at the monitor while adjusting the light and focus, as showed in Figure 4. The position of the cylinder on the table is marked with a marker, such that the cylinders can be easily rotated without loosing the position for which the cameras are calibrated.

Lighting and Focus Adjustments

With the cylinders at the marked position, the following main steps are taken for adjusting the final camera position, the camera exposure, artificial light and camera focus:

Figure 4: Experimental setup for the DIC measurements

1) Initial adjustments in artificial light and camera exposure time. The cameras are positioned according to their aperture size and available space in the lab, as discussed before. With the capture system on, the initial brightness is verified by adjusting the LED panel intensity and position. In the present experimental setup, the ambient light was enhanced by the LED panel. The camera exposure in the present study ranged from 20 to 150 ms, depending on the varying ambient light conditions that is described in the following paragraph.
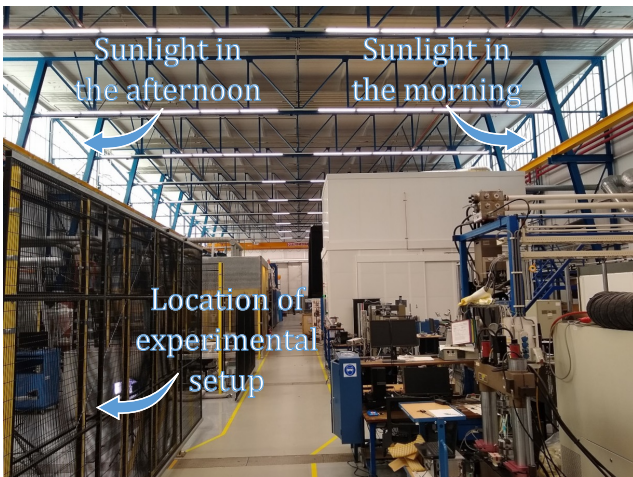

Figure 5: Delft Aerospace Structures and Materials Laboratory (DASML) ambient lighting. The varying light affects the measurements, requiring on-the-fly adjustments of artificial light and camera exposure time.

2) Positioning of cameras. With sufficient brightness the final positioning of the cameras is performed. The cameras are laterally moved and rotated along two axis to make the cylinders appear at the middle of the image with the length aligned with the vertical edges of the camera images. The fixed position is guarantees by screwing the adjustment bolts tightly.

3) Focus adjustment. The focus adjustment for a cylindrical surface requires finding a compromise between surface depth-coverage and accuracy, whereby the optimal focus is not adjusted to be at the outer-most face, but slightly deeper to allow more accuracy on surface points that are more in depth, as illustrated in Figure 6. Even with this compromise, the surface topography is less accurately captured for the points laying more in depth on the cylindrical shell, where the predicted pixel noise can increase up to 5%.
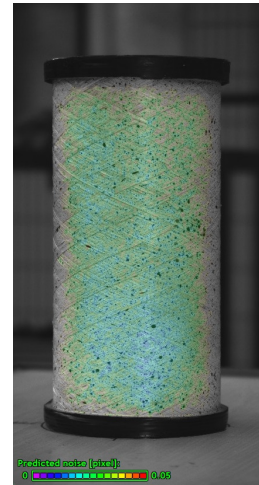

Figure 6: Adjusted focus with a compromise between accuracy and surface depth coverage.

4) Final brightness adjustment. Ideally, one should use a camera exposure as small as possible, with sufficient diffuse, ambient, light to provide sufficient brightness. However, the lighting devices usually result in non-diffuse focused light that on a cylindrical shell easily reflects to the cameras, which makes finding the perfect lighting conditions somewhat challenging, especially if the ambient light conditions vary during the experiments. For instance, in the Delft Aerospace Structures and Materials Laboratory (DASML) the sunlight switches from one side in the morning to the other side in the afternoon. Moreover, the light conditions changed quickly during the experiments due to sunlight intermittently blocked by passing clouds. Figure 5 illustrates. Future solutions for a better measurement setup could make use of a tent to minimize the effect of ambient light and additional LED panels to guarantee sufficient artificial light to outshine the ambient light. This would also have the benefit of allowing minimal exposure times, making the measurements less susceptible to disturbances, as in the cases of larger camera exposure times. The authors used the LED panel shown in Figure 4 to compensate these fast changing light conditions. It is worth mentioning that in the worst case one picture took 15 minutes to be taken, until sufficiently good brightness conditions were reached. Figure 7 compares the various brightness conditions, as presented by the VIC SNAP 3D software [30].
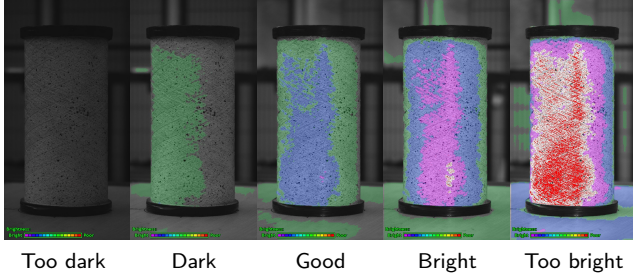
|Too dark|Dark|Good|Bright|Too bright|

Figure 7: DIC brightness conditions. Dark conditions are found if the exposure time is too small and there is no sufficient environmental light. focused light produces reflex on the cylindrical surface.

Calibrating the DIC System

The authors performed one calibration per measurement. Three measurements were performed per cylinder shown in Figure 2, resulting in 36 measurements. The calibration is highly affected by the focus adjustments explained earlier, such that before every calibration the focus must be checked and adjusted whenever necessary. The marked position of the cylinder on the table guarantees that the cylindrical shell remains in the region for which the focus was calibrated, which is crucial since the measurement process requires rotating the cylinder at every 60°. As illustrated in Figure 8, a calibration pattern of 5 mm is used and placed at 9 positions defining the extremities of the region of interest being measured. The calibration pattern is always rotated to follow the cylindrical surface to improve the accuracy of more in-depth measured points. The pixel error produced by the calibration procedure can be calculated, and among all measurements herein reported this error ranges from 0.014 pixels to 0.049 pixels. Along the 300 mm length of the cylinder there are approximately 3300 pixels, meaning 11 pixels per mm; hence, the expected measurement error ranges within 0.001 mm to 0.004 mm. This is the expected error in the region covered by the calibration patterns. Surface points laying beyond the calibrated area show larger errors and are ignored in the stitching procedure discussed next.

DIC Raw Data

The DIC raw data of the present work [31] consists on a cloud of points x_i, y_i, z_i for $i = 1, 2, \ldots, n_{points}$ representing the topography of the measured cylinders at each circumferential position, as illustrated Figure 9. All points are expressed in terms of the DIC coordinate system XYZ, depicted in Figure 9.

The location of the cylinders on the measurement table is fixed by circulating a marker pen around the cylinder. An arbitrary reference for the circumferential position that corresponds to the 0° angle is defined on the table. Meanwhile, all cylinders are marked at the resin potting region at every 60°, such that a total of 6 circumferential position markers are created. The DIC system is only calibrated once, when the cylinder is at the circumferential position 0°. While rotating the cylinder, we always check the brightness and focus

conditions, as explained earlier. One DIC picture is taken from each circumferential position, as illustrated in Figure 10. The next step consists on stitching the DIC measurements from the 6 faces into a closed topographic measurement of the entire cylinder. Note, as an example, that Degenhardt et al. [23] used a high-speed DIC setup consisting of 4 pairs of cameras synchronized for a complete coverage of the cylinder circumference, and obtaining up to 1000 images per second. A similar system could have been used to measured the mid-surface imperfection, but such hardware setup is considerably more costly than what is herein proposed.

4. Best-fitting the DIC raw data

For each stereo picture, a partial topography of the cylinder is obtained as a cloud of points. With the camera resolution 9 mega pixels herein adopted, a large sample of points was originally present, such that we only exported a ratio of 1 out of every 4 points along the horizontal and 1 out of ever 4 points along the vertical direction of each picture. Even with this sampling reduction, the data points are enough to discretize small geometric features that are orders of magnitude more refined than a typical finite element mesh used in studies with imperfection-insensitive cylindrical shells [18, 32].

With the aim to facilitate the later stitching steps and to create a standard format for all geometric imperfections, all DIC raw data points are transformed to a common reference frame. Figure 11 illustrates a cylindrical coordinate system adopted as the common reference frame for which the data points x_i, y_i, z_i are transformed to new coordinates x_c, y_c, z_c. The transformation is obtained according to the following relation:

$$\begin{Bmatrix} x_c \\ y_c \\ z_c \end{Bmatrix} = [R_z][R_y][R_x] \begin{Bmatrix} x_i + x_0 \\ y_i + y_0 \\ z_i + z_0 \end{Bmatrix} + \begin{Bmatrix} 0 \\ 0 \\ z_1 \end{Bmatrix} \quad (1)$$

where x_0, y_0, z_0 represent translation offsets before rotation, $[R_z][R_y][R_x]$ are rotation matrices, and z_1 is a translation offset applied after the rotation. It is important to mention that in Eq. 1 there are two separate translations, being the first before the rotation and the second after the rotation, along the axial direction. This two-step translation strategy proved to enable a significantly faster convergence of the surface fitting algorithm. The rotation matrices $[R_z][R_y][R_x]$ are given by Eqs. 2 − 4:

$$[R_x] = \begin{bmatrix} 1 & 0 & 0 \\ 0 & \cos\alpha & -\sin\alpha \\ 0 & \sin\alpha & \cos\alpha \end{bmatrix} \quad (2)$$

$$[R_y] = \begin{bmatrix} \cos\beta & 0 & \sin\beta \\ 0 & 1 & 0 \\ -\sin\beta & 0 & \cos\beta \end{bmatrix} \quad (3)$$
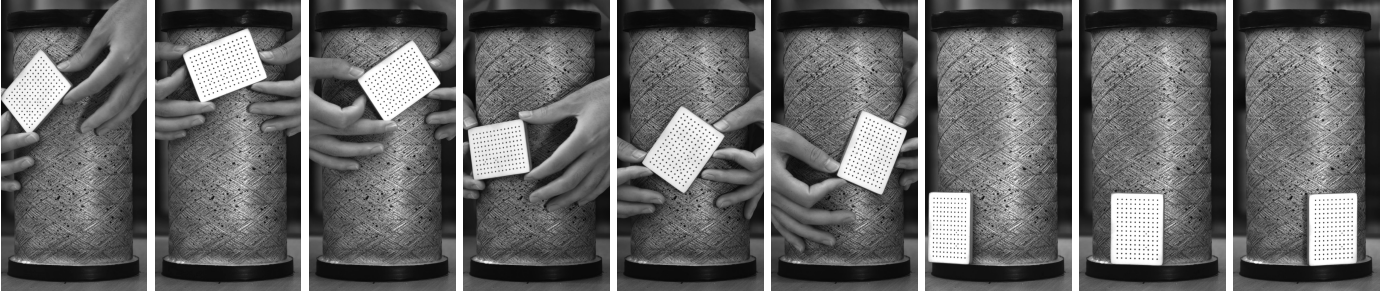
Figure 8: DIC calibration images for S1-1. The calibration pattern of 5 mm is placed at 9 positions defining the extremities of the region of interest.
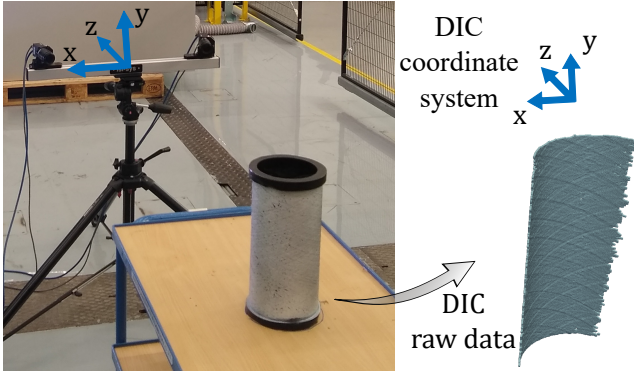

Figure 9: DIC coordinate system and example of raw data. The raw data consists of a topological representation of the cylinder outer surface, discretized by points.
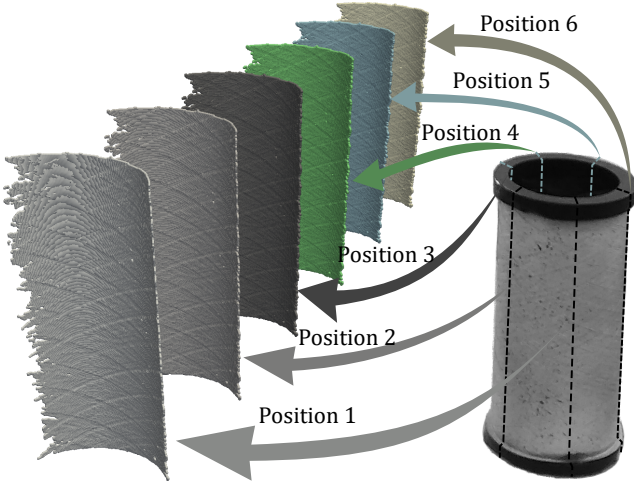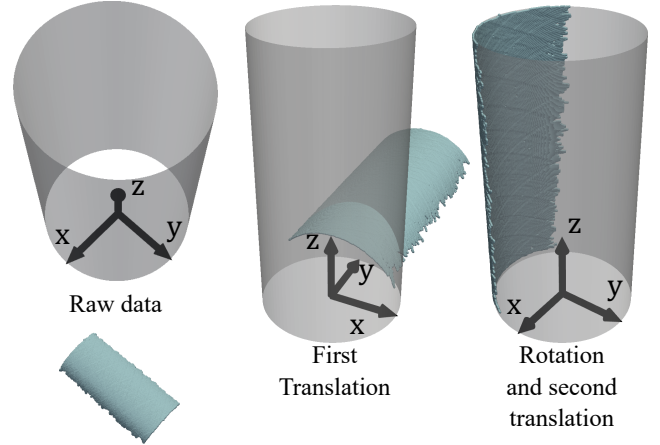

Figure 11: Best-fit cylinder. Each set of raw data measured at different positions is transformed to a reference cylinder defined using the DIC coordinate system of Fig. 9.

Figure 10: DIC raw data extracted at each circumferential position. All this data is obtained on the same coordinate system of Figure 9. All adjacent positions are 60° apart.

$$[R_z] = \begin{bmatrix} cos\gamma & -sin\gamma & 0 \\ sin\gamma & cos\gamma & 0 \\ 0 & 0 & 1 \end{bmatrix} \tag{4}$$

where α, β, γ are transformation angles respectively measured according to the right-hand rule around the x, y, z axes of Figure 11.

Equation 1 requires a total of 7 parameters $(\alpha, \beta, \gamma, x_0, y_0, z_0, z_1)$ to be found in order to transform the DIC raw data points x_i, y_i, z_i to points expressed in terms of the desired coordinate system x_c, y_c, z_c. For fitting a perfect cylinder, γ is not needed and can be ignored, e.g. by using $\gamma = 0$. The first best-fitting optimization given in Eq. 5 determines $\alpha, \beta, x_0, y_0, z_0$:

$$\begin{aligned} \text{minimize} \quad & \sum_{c=1}^{n_{points}} \sqrt{x_c^2 + y_c^2} - r_{cyl} \\ \text{with respect to} \quad & r_{cyl}, \alpha, \beta, x_0, y_0, z_0 \\ \text{subject to} \quad & r_{min} \leq r_{cyl} \leq r_{max} \\ & -\pi \leq \alpha, \beta, \gamma \leq +\pi \\ & -\infty \leq x_0, y_0, z_0 \leq +\infty \end{aligned} \tag{5}$$

where r_{cyl} can be allowed to vary between r_{min} and r_{max} or set to a constant value, and in the present study it is fixed at $r_{cyl} = 68$ *mm*, which is the size of the mandrel used to manufacture the VAFW cylinders. Similarly to Wang et al. [33], the optimization of Eq. 5 is solved using a nonlinear least-squares method, which in the case of the present study is the `scipy.optimize.least_squares` function available in SciPy [34].

Because of the focus not being uniform over the cylindrical surface, the authors noticed a larger error at the regions outside the center of the circumferential position being measured. By developing a best-fit elliptic cylinder equation, detailed in Appendix A, a higher accuracy is obtained during the imperfection stitching step. For the best-fit elliptic cylinder the transformation angle γ must be included as a design variable in the best-fit optimization. Thus, after the best-fit cylinder problem of Eq. 5 is solved with a constant value of r_{cyl}, the optimization step of Eq. 6 is included aiming to determine γ, a, b:

$$\text{minimize} \quad \sum_{c=1}^{n_{points}} \sqrt{x_c^2 + y_c^2} - r(\theta)$$

$$\text{with respect to} \quad \gamma, a, b \tag{6}$$

$$\text{subject to} \quad \begin{aligned} -\pi \leq \gamma \leq +\pi \\ 0.9 r_{cyl} \leq a, b \leq 1.1 r_{cyl} \end{aligned}$$

where $\theta = \arctan y_c / x_c$; the elliptical radius $r(\theta)$ is calculated with Eq. A.2; a, b are respectively the major and the minor radii of a best-fit elliptic cylinder, to be determined by the nonlinear least-squares optimizer.

The next best-fit step consists on calculating z_1 that is used in the coordinate transformation of Eq. 1, using the optimization of Eq. 7:

$$\text{minimize} \quad \sum_{c=1}^{n_{points}} \Delta z_c$$

$$\text{with respect to} \quad z_1 \tag{7}$$

$$\text{subject to} \quad -\infty \leq z_1 \leq +\infty$$

with Δz_c calculated using Eq. 8 that represents the sum of distances of all points laying outside the inner cylindrical shell domain delimited using the cylinder height H, and on the length of the resin potting l_p illustrated in Fig. 1.

$$\Delta z_c = \begin{cases} \Delta z_c = z_c - (H - l_p) & z_c > (H - l_p) \\ \Delta z_c = 0 & l_p < z_c < (H - l_p) \\ \Delta z_c = l_p - z_c & z_c < l_p \end{cases} \tag{8}$$

In a more general case the DIC raw data points might contain points that measure the position of the resin potting or even the table surface, therefore negatively affecting the best-fit step. To avoid the effect of spurious raw data points in the best-fit optimizations of Eq. 6 and 7, the DIC raw data points are clipped before the optimization with the following clipping box:

$$\begin{aligned} x_{min}, x_{max} &= -\infty, +\infty \\ y_{min}, y_{max} &= -130 \, mm, +120 \, mm \\ z_{min}, z_{max} \end{aligned} \tag{9}$$

where $z_{max} = (z_{imax} + 1)\,[mm]$ and $z_{min} = (z_{max} - R(1 - \cos 45°) - 1)\,[mm]$. The value z_{imax} is determined for each DIC raw data corresponding to one circumferential position, as shown in Figure 9. The limits y_{min}, y_{max} were chosen just enough remove spurious points from the resin potting. Despite the points outside the clipping box are ignored during the best-fit optimization steps, they also undergo the transformation given by Eq. 1 and are kept for the next stitching steps.

4.1. Stitching methodology

After best-fitting the DIC raw data points to the desired coordinate system illustrated in Figure 11, each measurement is rotated to its nominal circumferential position, as illustrated in Figure 12. One could try to simply trim the point data of each position in order to achieve a three-dimensional topography pattern, but without a proper stitching algorithm, the outcome would be what is illustrated in Figure 13a. In order to achieve a correctly stitched three-dimensional imperfection pattern, as is illustrated in Figure 13b, we propose an automated stitching scheme.
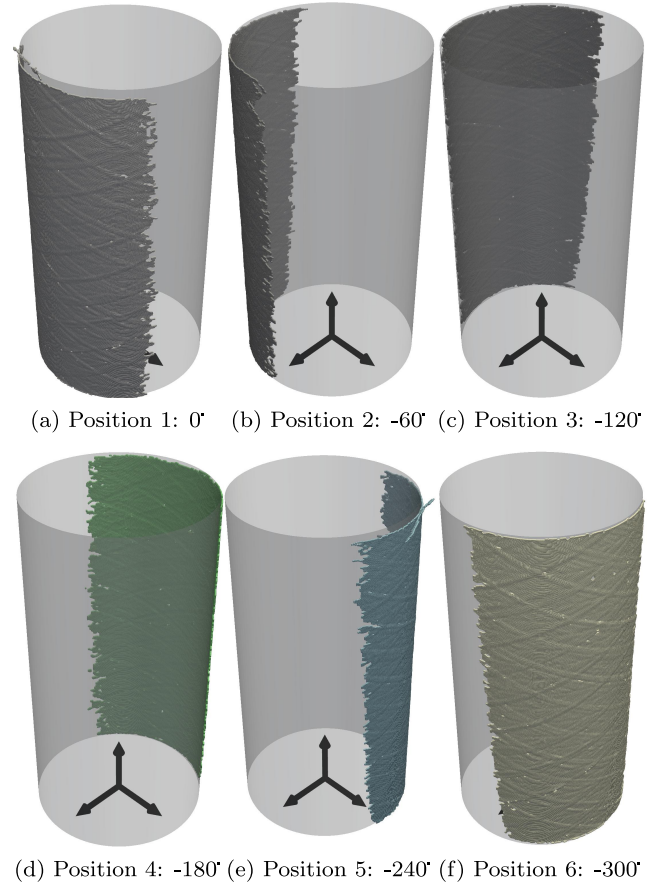

(a) Position 1: 0˚ (b) Position 2: -60˚ (c) Position 3: -120˚

(d) Position 4: -180˚ (e) Position 5: -240˚ (f) Position 6: -300˚

Figure 12: Initial rotation of each DIC transformed data onto their nominal position.

Each pair of adjacent DIC measurements, named positions i and $i+1$, are stitched separately. A probing line is defined at the circumferential position that corresponds to the frontier between positions i and $i+1$. For instance, between
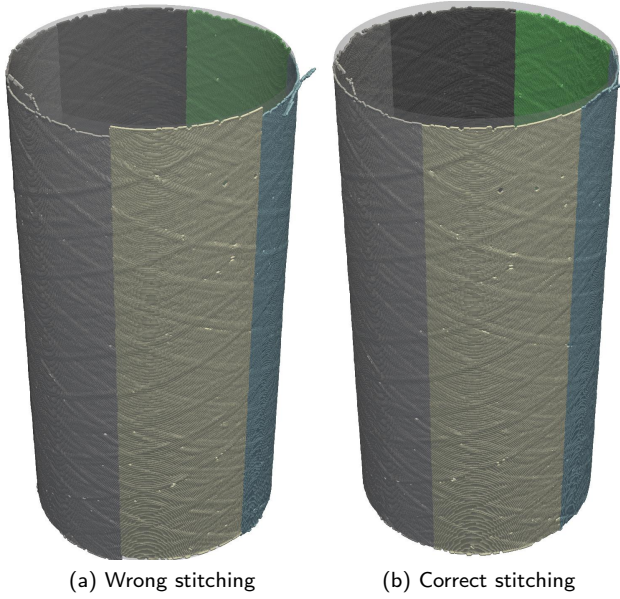
(a) Wrong stitching   (b) Correct stitching

Figure 13: Comparison between a wrong and a correct stitching. The wrong stitching is simply achieved by rotating and trimming. The correct stitching requires rotating, adjusting according to the optimization given in Eq. 10, and finally trimming.

positions 1 and 2 the probing line is located at $-30°$; between 2 and 3 at $-90°$ and so forth. The probing line is located at a coordinate that corresponds to the mid-surface, here assumed to be at the mean value of all $r_c = \sqrt{x_c^2 + y_c^2}$, with r_c representing the radial coordinates of all points among positions i and $i + 1$. During the stitching process, the points belonging to position $i + 1$ are adjusted circumferentially by a value $\Delta\theta_{i+1}$ and longitudinally by a value Δz_{i+1}, according to the optimization of Eq. 10:

$$\text{minimize} \quad \sum_{i=1}^{n_p} \left(\Delta r_i - \Delta r_{i+1}\right)^2$$

$$\text{with respect to} \quad \Delta\theta_{i+1}, \Delta z_{i+1} \tag{10}$$

$$\text{subject to} \quad -10° \leq \Delta\theta_{i+1} \leq +10°$$
$$-10\ mm \leq \Delta z_{i+1} \leq +10\ mm$$

where n_p is the number of points along the probing line, here fixed at $n_p = 1000$; $\Delta r_i, \Delta r_{i+1}$ are the out-of-plane distances between the probing line and the positions i and $i+1$, respectively. Figure 14 illustrates the stitching variables $\Delta\theta_{i+1}, \Delta z_{i+1}$, and a plot of Δr_i and Δr_{i+1}. For each measured cylinder consisting of the 6 DIC circumferential data points illustrated in Figure 10, the optimization of Eq. 10 is run six times. First, position 1 is taken as a reference (Figure 15a) and the first stitching optimization finds $\Delta\theta_2, \Delta z_2$ (Figure 15b), this is progressively done until the final stitching step that finds the adjustment necessary for position 1, $\Delta\theta_2$ and Δz_2, to perfectly close the 3D imperfection pattern. At
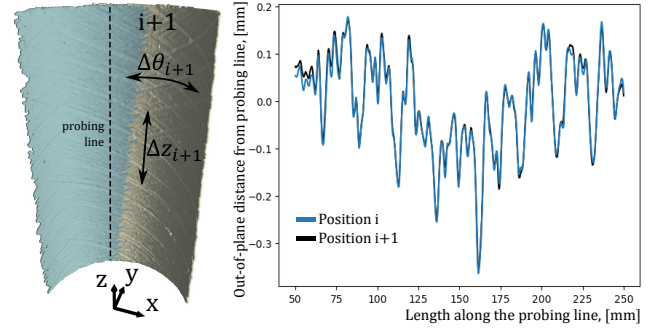

Figure 14: Variables $\Delta\theta_{i+1}$ and Δz_{i+1} used to adjust position $i+1$ in order to minimize the difference of out-of-plane distance between positions i and $i + 1$, measured from the probing line.

the end, all $\Delta\theta_i$ and Δz_i, for $i = 2, 3, 4, 5, 6$ can be offset such that $\Delta\theta_1 = 0$ and $\Delta z_1 = 0$.

The initial guess consisting of θ_i, z_i in the optimization of Eq. 10 significantly influences the optimized output, such that for each case θ_i, z_i is found after searching 121 equally spaced initial points, consisting of a combination of circumferential offset values ranging from $-10°$ to $+10°$, and axial offset values ranging from $-20\ mm$ to $+20\ mm$. The best initial guess is determined by finding the initial point θ_i, z_i that resulted in the minimum value of $\sum_{i=1}^{n_p} \left(\Delta r_i - \Delta r_{i+1}\right)^2$, which is the same function being minimized in the optimization described in Eq. 10.

5. Stitching Results

The inner mould used during the filament winding process has a smooth surface, resulting in a very low imperfection signature at this region. Figure 16 shows the inner surface of cylinder VAT2-2, where the different tows orientations can be seen. Assuming a smooth inner surface, the three-dimensional stitched outer-surface topology can be used to calculate the thickness imperfection patterns generated by the filament winding manufacturing process. Figures 18 – 21 show the stitched imperfections for the VAFW cylinders of Figure 2. The geometric imperfections were measured in triplicate in order to evaluate the variability of the proposed technique. The results are available in a public dataset [35].

Figure 17 shows the average thickness $h_{avg}(z)$ calculated over the longitudinal coordinate $25\ mm \leq z \leq 275\ mm$ for one sample of each cylinder design. The longitudinal length close to the edges was not considered due to the resin potting. The exact mass of each cylinder can be calculated using Eq. 11. By assuming a representative $h_{avg}(z)$ distribution the mass can be approximated as per Eq. 12; where the ratio 300/250 must be used to compensate for the missing region close to the edges; $\rho = 1600\ kg/m^3$ is the mass density of the cylinders; and $r_{cyl} = 68\ mm$ is the cylinder mould radius. Table 1 shows the calculated mass for all reconstructed geometric imperfections. The columns m_1, m_2, m_3 represent the three DIC measurements performed in each sample. The standard deviation of the calculated mass is extremely small, achieving a maximum of $\pm0.03\ g$. The real masses measured

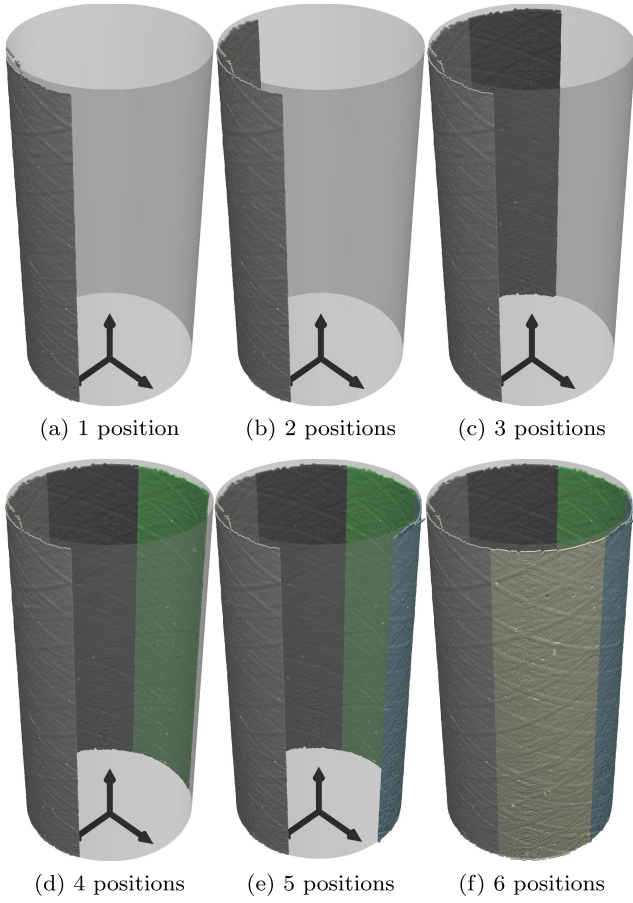(a) 1 position   (b) 2 positions   (c) 3 positions

(d) 4 positions   (e) 5 positions   (f) 6 positions

Figure 15: Initial rotation of each DIC transformed data onto their nominal position.

Figure 16: Inner surface of filament-wound cylinder VAT2-2. The smooth mould produced a significantly smoother surface compared to the outer surface.

Figure 17: Average thickness distributions $h_{avg}(z)$ for different VAFW designs.

after manufacturing are also given, and the proximity of the calculated masses to the real masses show the high accuracy of the proposed methodology to achieve the reconstructed geometric imperfections.

$$m_{cyl} = \int_{z=0\ mm}^{300\ mm} \int_{\theta=0}^{2\pi} \int_{r=r_{cyl}}^{r_{cyl}+h(r,\theta)} \rho r\, dr\, d\theta\, dz \quad (11)$$

$$m_{cyl} \approx 2\pi r_{cyl}\rho \frac{300}{250} \int_{z=25\ mm}^{z=275\ mm} h_{avg}(z)\, dz \quad (12)$$

6. Conclusions

We presented a novel methodology to obtain the geometric imperfection pattern of composite shells of revolution by means of digital image correlation (DIC) using a simple experimental setup that involves only one pair of cameras. DIC is largely applied as a technique to measure displacement and strain fields, and the present study is the first one to extend the applicability of this technique towards imperfection measurements and formalize a procedure to reconstruct the three-dimensional imperfection pattern.
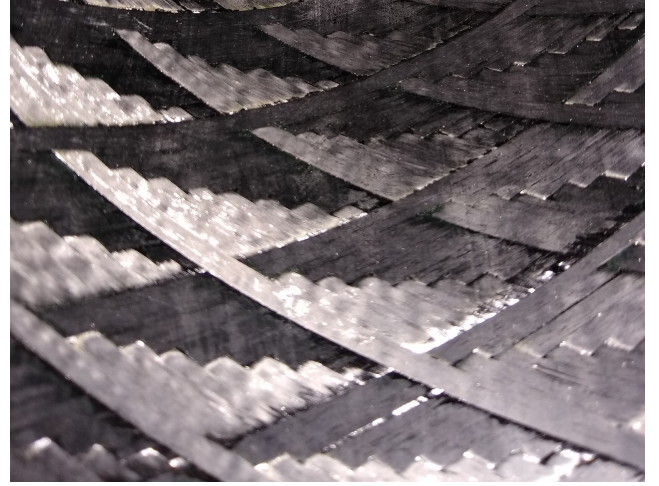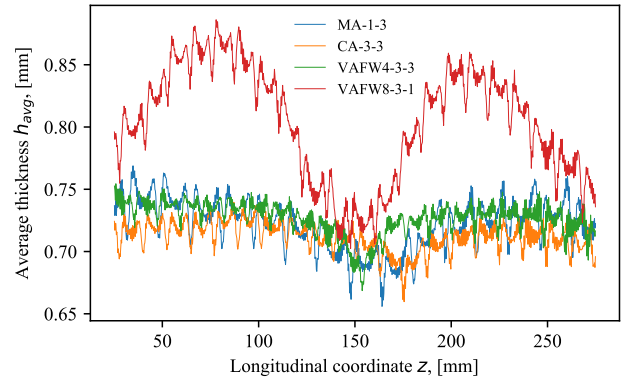
The methodology herein proposed is applicable to any shell of revolution and assumes that the inner mold surface is smooth, making the approach applicable to filament-wound structures, and a large class of shells manufactured by means of a smooth inner mold.

Future studies should focus on uncertainty quantification and reliability-based analyses to assess the sensitivity of the stability behavior of variable-angle filament-wound (VAFW) shells to the error of the imperfection measurement technique herein proposed, and preferably cross-checking with other imperfection measurement techniques, for small and large structures.
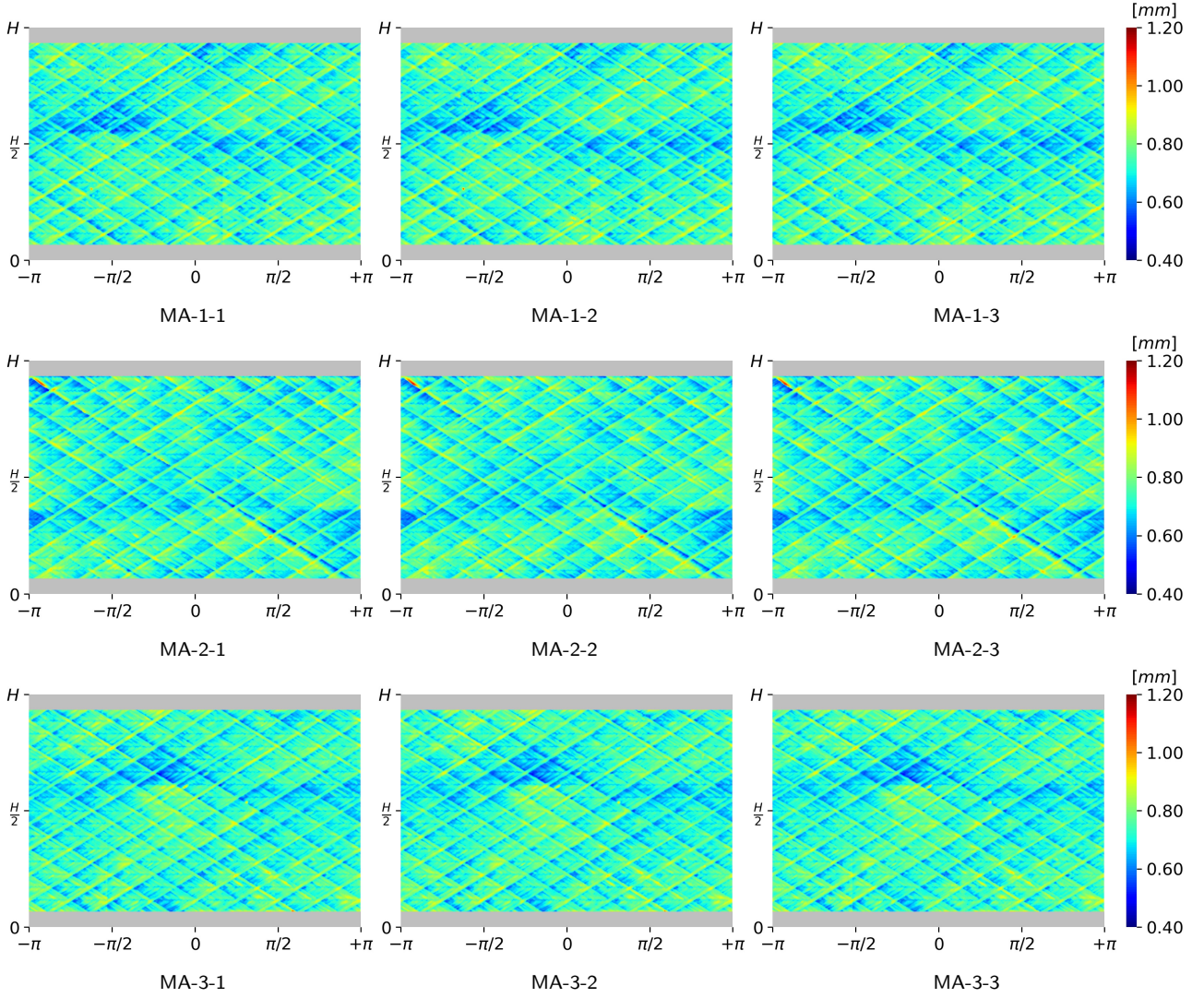
Acknowledgements

Figure 18: Stitched thickness imperfection for MA-, three measurements.

DASML DIC system.

CRediT authorship contribution statement

Saullo G. P. Castro: Conceptualization, methodology, software, formal analysis, investigation, validation, data curation, supervision, resources, writing - original draft preparation. **José Humberto S. Almeida Jr.:** Formal analysis, investigation, funding acquisition, writing - original draft preparation, writing - reviewing and editing. **Luc St-Pierre:** Writing - reviewing and editing, resources. **Zhihua Wang:** Investigation, methodology.

A. Elliptic cylinder

For a better stitching of the imperfection data, the input cloud of points can be adjusted to an elliptic cylinder instead of a cylinder. Using the coordinate system of Figure 11, the perfect elliptic perimeter can be represented in Cartesian co-

ordinates as:

$$\frac{x^2}{a^2} + \frac{y^2}{b^2} = 1 \tag{A.1}$$

where x, y are points laying perfectly on the ellipse surface, a is the major and b the minor radii of the ellipse. Replacing the polar relations:

$$x = r(\theta)\cos\theta \qquad\qquad y = r(\theta)\sin\theta$$

into Eq. A.1 leads to the expression of the perfect ellipse radius $r(\theta)$:

$$r(\theta) = \frac{ab}{\sqrt{(a\sin\theta)^2 + (b\cos\theta)^2}} \tag{A.2}$$

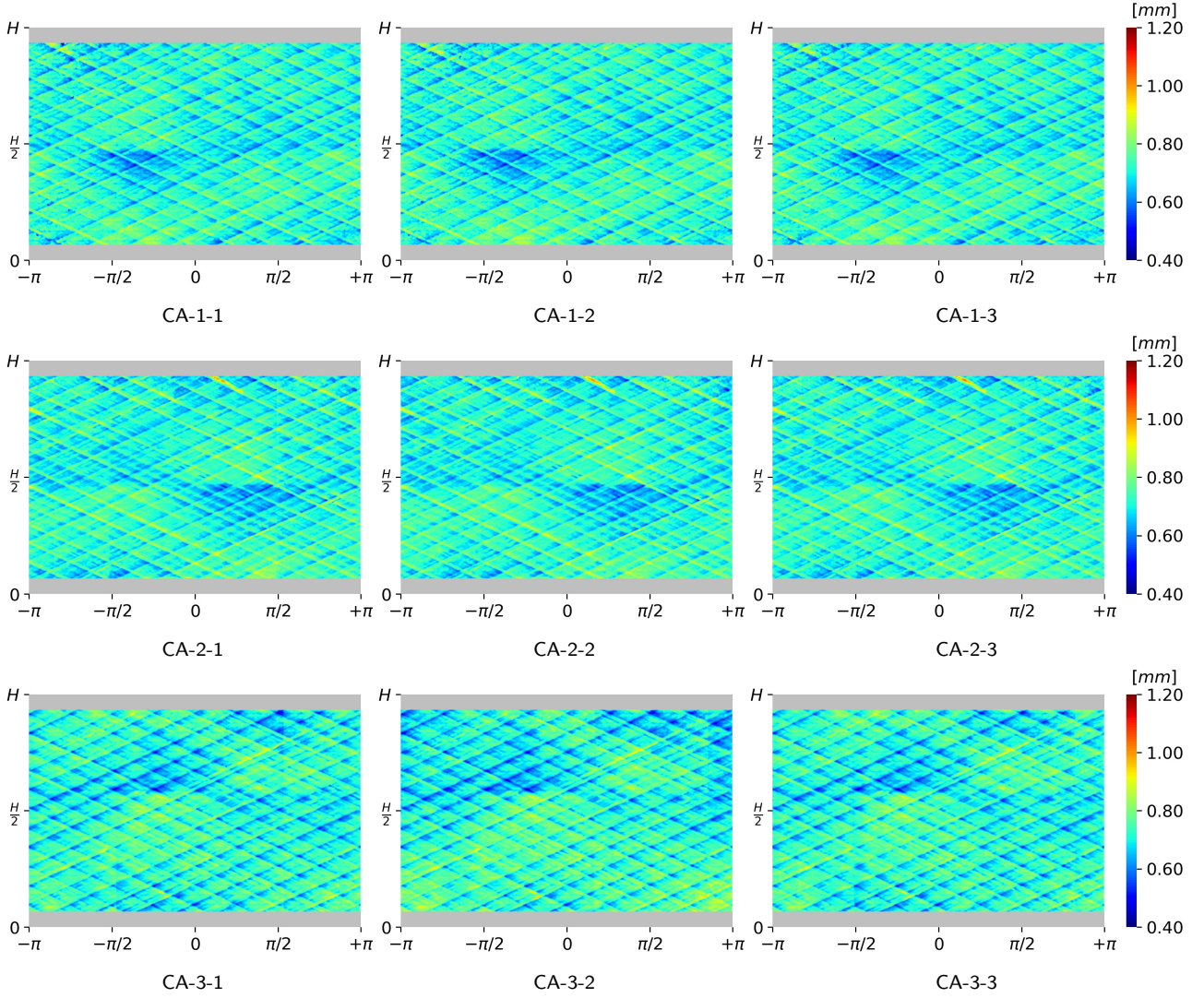For a cloud of measured DIC points transformed to x_c, y_c, z_c according to Eq. 1, the measured radius of each

Figure 19: Stitched thickness imperfection for CA-, three measurements.

point, r_c, and its corresponding circumferential position θ_c, can be calculated as:

$$\theta_c = \tan^{-1}\left(y_c/x_c\right)$$
$$r_c = \sqrt{x_c^2 + y_c^2} \tag{A.3}$$

It is expected that the measured radius r_c differs from the perfect elliptic cylinder radius of the corresponding circumferential position θ_c, and this difference consists of a geometric imperfection for this data point, here represented by Δr_c:

$$\Delta r_c = r_c - r(\theta_c) \tag{A.4}$$

This imperfection value can be remapped to a best-fit cylinder, as the one illustrated in Figure 11, by adding the geometric imperfection to the best-fit radius, such that a new radial position r_c is calculated:

$$r_{cnew} = R + \Delta r_c \tag{A.5}$$

Finally, one can retrieve the new Cartesian coordinates for each data point using:

$$x_{cnew} = r_{cnew}\cos\theta_c$$
$$y_{cnew} = r_{cnew}\sin\theta_c \tag{A.6}$$
$$z_{cnew} = z_c$$

References

[1] J. Arbocz, M. W. Hilburger, Toward a Probabilistic Preliminary Design Criterion for Buckling Critical Composite Shells, AIAA Journal 43 (8) (2005) 1823–1827. doi:10.2514/1.11368.

[2] M. W. Hilburger, M. P. Nemeth, J. H. Starnes, Shell Buckling Design Criteria Based on Manufacturing Imperfection Signatures, AIAA JOURNAL 44 (3) (2006) 654–663. doi:10.2514/1.5429.

[3] J. G. Croll, Towards a rationally based elastic-plastic shell buckling design methodology, Thin-Walled Structures 23 (1-4) (1995) 67–84. doi:10.1016/0263-8231(95)00005-X.

[4] R. V. Southwell, On the general theory of elastic stability, Philosoph-
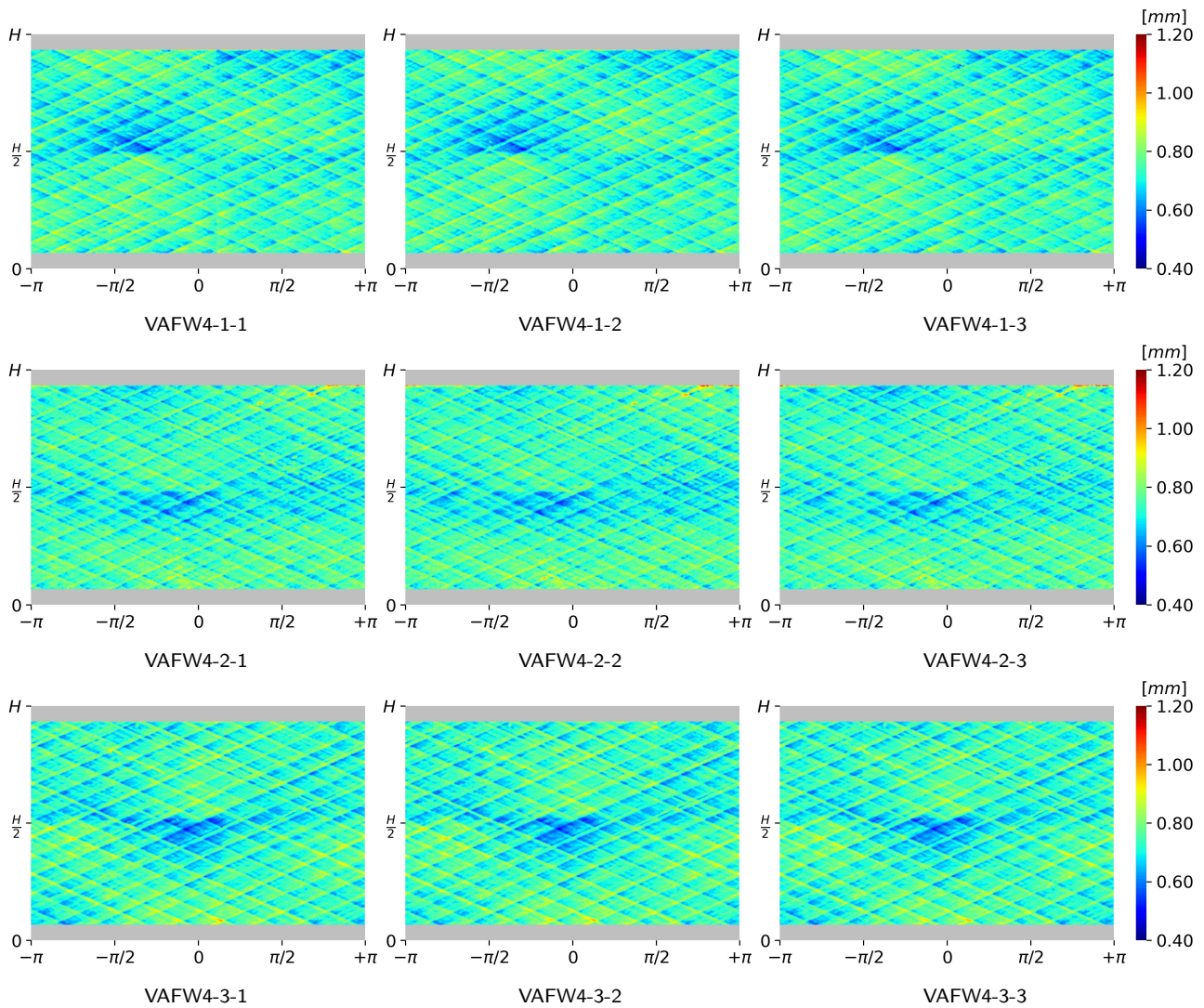
Figure 20: Stitched thickness imperfection for VAFW4-, three measurements.

ical Transactions of the Royal Society of London. Series A 213 (497-508) (1914) 187–244. doi:10.1098/rsta.1914.0005.

[5] W. Flügge, Die Stabilität der Kreiszylinderschale, Ingenieur-Archiv 3 (5) (1932) 463–506. doi:10.1007/BF02079822.

[6] L. H. Donnell, A New Theory for the Buckling of Thin Cylinders Under Axial Compression and Bending, ASME Transactions 56 (1934) 795–806.

[7] T. Von Kármán, H.-S. Tsien, The Buckling of Thin Cylindrical Shells Under Axial Compression, Journal of the Aeronautical Sciences 8 (8) (1941) 303–312. doi:10.2514/8.10722.

[8] W. T. Koiter, On the stability of elastic equilibrium, Ph.D. thesis, Polytechnic Institute of Delft, Delft, the Netherlands (1945).

[9] J. Peterson, P. Seide, V. Weingarten, Buckling of thin-walled circular cylinders - NASA SP-8007, Tech. rep., NASA, Virginia, USA (1968). URL https://ntrs.nasa.gov/citations/19690013955

[10] I. Sheinman, G. J. Simitses, Buckling and postbuckling of imperfect cylindrical shells under axial compression, Computers and Structures 17 (2) (1983) 277–285. doi:10.1016/0045-7949(83)90016-0.

[11] G. J. Simitses, D. Shaw, I. Sheinman, Imperfection sensitivity of laminated cylindrical shells in torsion and axial compression, Composite Structures 4 (4) (1985) 335–360. doi:10.1016/0263-8223(85)90032-7.

[12] D. J. Wilkins, T. S. Love, Combined compression-torsion buckling tests of lamianted composite cylindrical shells, in: AIAA/ASME/SAE 15th Structures, Structural Dynamics and Materials Conference, AIAA, ASME, SAE, Las Vegas, Nevada, USA, 1974, pp. 1–8. doi:10.1016/0263-8223(85)90032-7.

[13] M. K. Chryssanthopoulos, V. Giavotto, C. Poggi, Characterization of manufacturing effects for buckling-sensitive composite cylinders, Composites Manufacturing 6 (2) (1995) 93–101. doi:10.1016/0956-7143(95)99649-D.

[14] J. Arbocz, C. D. Babcock, Prediction of Buckling Loads Based on Experimentally Measured Initial Imperfections, in: Buckling of Structures, Springer Berlin Heidelberg, 1976, pp. 291–311. doi:10.1007/978-3-642-50992-6{_}24.

[15] C. Bisagni, Numerical analysis and experimental correlation of composite shell buckling and post-buckling, Composites Part B: Engineering 31 (8) (2000) 655–667. doi:10.1016/S1359-8368(00)00031-7.

[16] N. Khot, V. Venkayya, Effect of fiber orientation on initial postbuckling behavior and imperfection sensitivity of composite cylindrical shells, Tech. rep. (1970).

[17] F. Taheri-Behrooz, M. Omidi, M. M. Shokrieh, Experimental and numerical investigation of buckling behavior of composite cylinders with cutout, Thin-Walled Structures 116 (2017) 136–144. doi:10.1016/j.tws.2017.03.009.
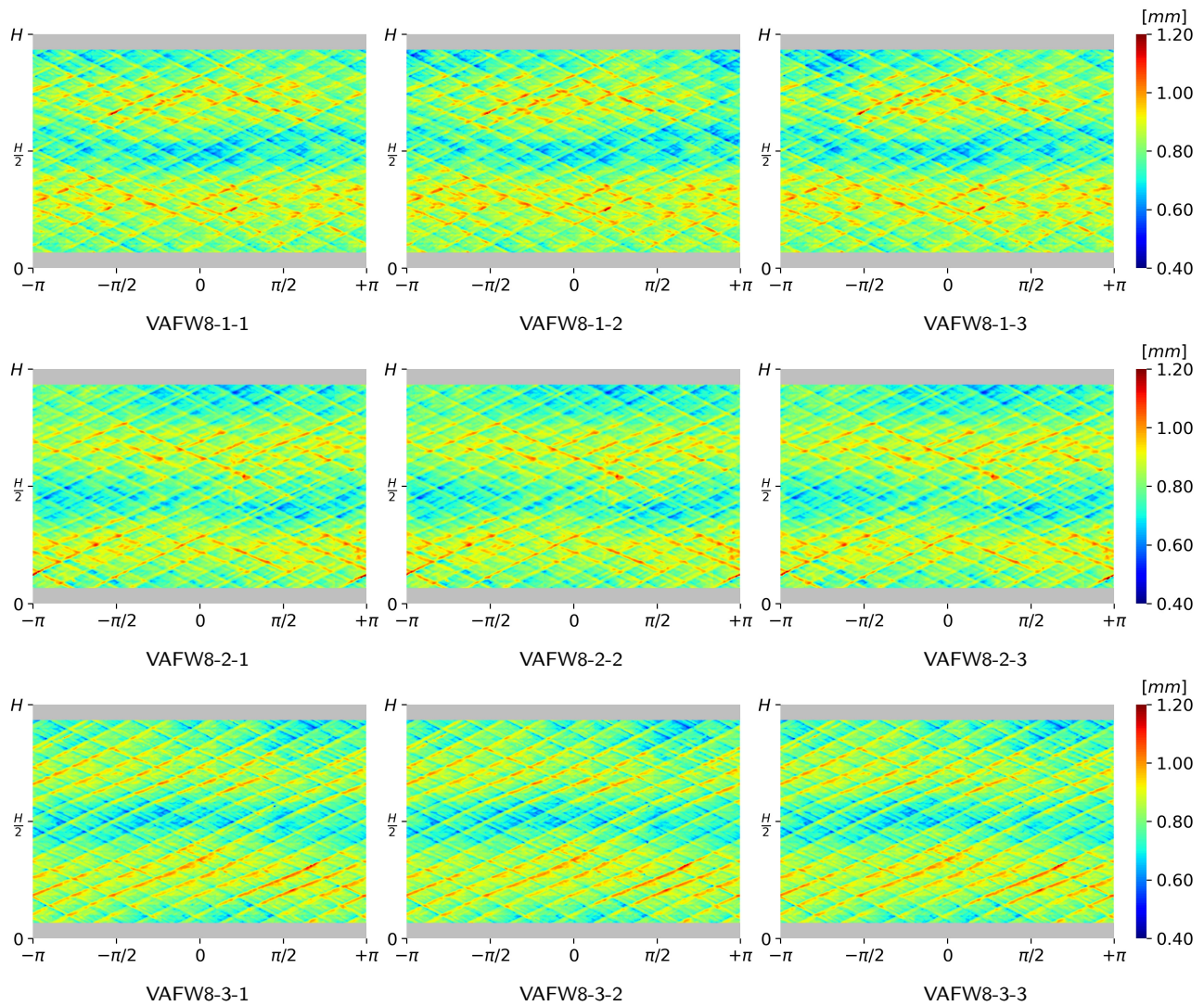
Figure 21: Stitched thickness imperfection for VAFW8-, three measurements.

[18] S. G. Castro, R. Zimmermann, M. A. Arbelo, R. Khakimova, M. W. Hilburger, R. Degenhardt, Geometric imperfections and lower-bound methods used to calculate knock-down factors for axially compressed composite cylindrical shells, Thin-Walled Structures 74 (2014) 118–132. doi:10.1016/j.tws.2013.08.011.

[19] C. Hühne, R. Rolfes, E. Breitbach, J. Teßmer, Robust design of composite cylindrical shells under axial compression - Simulation and validation, Thin-Walled Structures 46 (7-9) (2008) 947–962. doi:10.1016/j.tws.2008.01.043.

[20] S. G. Castro, R. Zimmermann, M. A. Arbelo, R. Degenhardt, Exploring the constancy of the global buckling load after a critical geometric imperfection level in thin-walled cylindrical shells for less conservative knock-down factors, Thin-Walled Structures 72 (2013) 76–87. doi:10.1016/j.tws.2013.06.016.

[21] Z. Wang, J. Almeida Jr, L. St-Pierre, Z. Wang, S. G. Castro, Reliability-based buckling optimization with an accelerated Kriging metamodel for filament-wound variable angle tow composite cylinders, Composite Structures 254 (2020) 112821. doi:10.1016/j.compstruct.2020.112821.

[22] M. F. Di Pasqua, R. Khakimova, S. G. Castro, M. A. Arbelo, A. Riccio, A. Raimondo, R. Degenhardt, Investigation on the Geometric Imperfections driven Local Buckling Onset in Composite Conical Shells, Applied Composite Materials 23 (4) (2016) 879–897. doi:10.1007/s10443-016-9490-7.

[23] R. Degenhardt, A. Kling, H. Klein, W. Hillger, H. C. Goetting, R. Zimmermann, K. Rohwer, A. Gleiter, Experiments on buckling and postbuckling of thin-walled CFRP structures using advanced measurement systems, International Journal of Structural Stability and Dynamics 07 (02) (2007) 337–358. doi:10.1142/S0219455407002253.

[24] R. Khakimova, S. G. Castro, D. Wilckens, K. Rohwer, R. Degenhardt, Buckling of axially compressed CFRP cylinders with and without additional lateral load: Experimental and numerical investigation, Thin-Walled Structures 119 (2017) 178–189. doi:10.1016/j.tws.2017.06.002.

[25] D. J. Eberlein, Composite Cylindrical Shell Buckling: Simulation & Experimental Correlation, Ph.D. thesis, Delft University of Technology (2019).
URL http://resolver.tudelft.nl/uuid:cbaf7f4f-ae81-4f54-ab75-c830d8c5cf6e

[26] E. Skukis, O. Ozolins, J. Andersons, K. Kalnins, M. A. Arbelo, Applicability of the vibration correlation technique for estimation of the buckling load in axial compression of cylindrical isotropic shells with and without circular cutouts, Shock and Vibration 2017 (11 2017). doi:10.1155/2017/2983747.

Table 1
Masses in [g] of each cylinder calculated from the reconstructed imperfection data. The values m_{real} represent the real masses of each cylinder measured after manufacturing.

Cylinder	m_{real}	m_1	m_2	m_3	$m_{avg} \pm \sigma_{m_{avg}}$
MA-1		148.05	148.06	148.08	148.06 ± 0.01
MA-2	148	148.13	148.18	148.14	148.15 ± 0.02
MA-3		148.03	148.07	148.05	148.05 ± 0.02
CA-1		146.04	146.07	146.06	146.06 ± 0.01
CA-2	146	145.97	145.98	145.97	145.97 ± 0.01
CA-3		145.97	145.97	145.97	145.97 ± 0.00
VAFW4-1		149.01	149.02	149.03	149.02 ± 0.01
VAFW4-2	149	149.12	149.16	149.10	149.13 ± 0.03
VAFW4-3		149.07	149.08	149.02	149.06 ± 0.03
VAFW8-1		164.77	164.77	164.77	164.77 ± 0.00
VAFW8-2	165	164.67	164.66	164.65	164.66 ± 0.01
VAFW8-3		164.71	164.71	164.69	164.70 ± 0.01

[27] E. Labans, C. Bisagni, Buckling and free vibration study of variable and constant-stiffness cylindrical shells, Composite Structures 210 (2019) 446–457. doi:10.1016/j.compstruct.2018.11.061.

[28] C. B. Azevedo, J. Almeida Jr., H. F. Flores, F. Eggers, S. C. Amico, Influence of mosaic pattern on hygrothermally-aged filament wound composite cylinders under axial compression, Journal of Composite Materials 54 (19) (2020) 2651–2659. doi:10.1177/0021998319899144.

[29] J. H. S. Almeida Jr, L. St-Pierre, Z. Wang, M. L. Ribeiro, R. Volnei Tita, S. C. Amico, S. G. Castro, Design, modeling, optimization, manufacturing and testing of variable-angle filament-wound cylinders, Preprint (2021).

[30] DIC Systems - isi-sys (2020).
URL http://www.isi-sys.com/category/products/dic-systems/

[31] S. G. P. Castro, J. H. S. Almeida Jr., VAFW cylinders 2020, S1, S2, S4, S8, DIC raw data. (Version 2021-02-01) [Data set]. (Feb. 2021). doi:10.5281/zenodo.4488797.

[32] S. G. P. Castro, J. Reichardt, E. Lozano, DESICOS Plug-in for Abaqus (Feb. 2021). doi:10.5281/zenodo.4506587.

[33] B. Wang, S. Zhu, P. Hao, X. Bi, K. Du, B. Chen, X. Ma, Y. J. Chao, Buckling of quasi-perfect cylindrical shell under axial compression: A combined experimental and numerical investigation, International Journal of Solids and Structures 130-131 (2018) 232–247. doi:10.1016/j.ijsolstr.2017.09.029.

[34] P. Virtanen, R. Gommers, T. E. Oliphant, M. Haberland, T. Reddy, D. Cournapeau, E. Burovski, P. Peterson, W. Weckesser, J. Bright, S. J. van der Walt, M. Brett, J. Wilson, K. J. Millman, N. Mayorov, A. R. J. Nelson, E. Jones, R. Kern, E. Larson, C. J. Carey, İ. Polat, Y. Feng, E. W. Moore, J. VanderPlas, D. Laxalde, J. Perktold, R. Cimrman, I. Henriksen, E. A. Quintero, C. R. Harris, A. M. Archibald, A. H. Ribeiro, F. Pedregosa, P. van Mulbregt, SciPy 1.0 Contributors, SciPy 1.0: Fundamental Algorithms for Scientific Computing in Python, Nature Methods 17 (2020) 261–272. doi:10.1038/s41592-019-0686-2.

[35] S. G. P. Castro, J. H. S. ALmeida Jr., VAFW cylinders 2020, S1, S2, S4, S8, stitched imperfections. (Version 2021-03-04) [Data set]. (Mar. 2021). doi:10.5281/zenodo.4581164.